

## Interface-induced perpendicular magnetic anisotropy of Co nanoparticles on single-layer h-BN/Pt(111)

Takahiro Watanabe, Yoichi Yamada, Akihiro Koide, Shiro Entani, Songtian Li, Zakhar I. Popov, Pavel B. Sorokin, Hiroshi Naramoto, Masahiro Sasaki, Kenta Amemiya, and Seiji Sakai

Citation: *Appl. Phys. Lett.* **112**, 022407 (2018); doi: 10.1063/1.5010836

View online: <https://doi.org/10.1063/1.5010836>

View Table of Contents: <http://aip.scitation.org/toc/apl/112/2>

Published by the [American Institute of Physics](#)

---

### Articles you may be interested in

[Giant tunnel magnetoresistance in polycrystalline magnetic tunnel junctions with highly textured MgAl<sub>2</sub>O<sub>4</sub>\(001\) based barriers](#)

*Applied Physics Letters* **112**, 022408 (2018); 10.1063/1.5013076

[Modulated spin orbit torque in a Pt/Co/Pt/YIG multilayer by nonequilibrium proximity effect](#)

*Applied Physics Letters* **112**, 022402 (2018); 10.1063/1.5006115

[Influence of MgO barrier quality on spin-transfer torque in magnetic tunnel junctions](#)

*Applied Physics Letters* **112**, 022406 (2018); 10.1063/1.5005893

[Characterization of spin-transfer-torque effect induced magnetization dynamics driven by short current pulses](#)

*Applied Physics Letters* **112**, 022401 (2018); 10.1063/1.5011721

[X-ray magnetic circular dichroism discloses surface spins correlation in maghemite hollow nanoparticles](#)

*Applied Physics Letters* **112**, 022404 (2018); 10.1063/1.5006153

[Localized surface plasmon resonance enhanced magneto-optical Kerr effect in Ni<sub>80</sub>Fe<sub>20</sub> thin films coated with Au nanorods](#)

*Applied Physics Letters* **112**, 022403 (2018); 10.1063/1.5011980

---



**Sensors, Controllers, Monitors**

from the world leader in cryogenic thermometry



## Interface-induced perpendicular magnetic anisotropy of Co nanoparticles on single-layer h-BN/Pt(111)

Takahiro Watanabe,<sup>1,2,3</sup> Yoichi Yamada,<sup>1,3,a)</sup> Akihiro Koide,<sup>4</sup> Shiro Entani,<sup>2,3,5</sup> Songtian Li,<sup>2,3</sup> Zakhar I. Popov,<sup>5</sup> Pavel B. Sorokin,<sup>3,5,6</sup> Hiroshi Naramoto,<sup>2</sup> Masahiro Sasaki,<sup>1,3</sup> Kenta Amemiya,<sup>7</sup> and Seiji Sakai<sup>1,2,3,a)</sup>

<sup>1</sup>*Institute of Applied Physics, University of Tsukuba, 1-1-1 Tennodai, Tsukuba, Ibaraki 305-8571, Japan*

<sup>2</sup>*Quantum Beam Science Research Directorate, National Institutes for Quantum and Radiological Science and Technology QST, 2-4 Shirakata, Tokai, Naka, Ibaraki 319-1106, Japan*

<sup>3</sup>*QST Future Laboratory, National Institutes for Quantum and Radiological Science and Technology QST, 2-4 Shirakata, Tokai, Naka, Ibaraki 319-1106, Japan*

<sup>4</sup>*Department of Materials Molecular Science, Institute for Molecular Science, 38 Nishigo-Naka, Myodaiji-cho, Okazaki, Aichi 444-8585, Japan*

<sup>5</sup>*National University of Science and Technology MISiS, 4 Leninskiy prospekt, Moscow 119049, Russia*

<sup>6</sup>*Technological Institute for Superhard and Novel Carbon Materials, 7a Centralnaya Street, Troitsk, Moscow 108840, Russia*

<sup>7</sup>*Photon Factory, High Energy Accelerator Research Organization KEK, Institute of Materials Structure Science, 1-1 Oho, Tsukuba, Ibaraki 305-0801, Japan*

(Received 27 October 2017; accepted 23 December 2017; published online 9 January 2018)

Ferromagnetism with perpendicular magnetic anisotropy (PMA) was observed at room temperature in cobalt nanoparticles (NPs) grown on hexagonal boron nitride (h-BN) on a Pt(111) surface. It was shown that the Co NPs have planar hexagonal shapes with a mean diameter of  $\sim 20$  nm and a mean height of  $\sim 1.6$  nm. The depth-resolved analysis of X-ray magnetic circular dichroism at the Co  $L_{2,3}$ -edges revealed that in the ferromagnetic Co NPs, the ratio of the orbital magnetic moment to the spin magnetic moment in the out-of-plane direction becomes larger at the Co NP/h-BN interface than the ratio in bulk Co. The B and N  $K$ -edge near edge X-ray absorption fine structures showed the orbital hybridization between the  $\pi$  orbitals of h-BN and d orbitals of Co at the interface, as an origin of the orbital magnetic moment enhancement possibly giving rise to PMA in the Co NPs. *Published by AIP Publishing.* <https://doi.org/10.1063/1.5010836>

The interfaces between ferromagnetic (FM) materials and atomic layer (AL) materials have attracted broad interest due to their particular importance in developing future spintronic devices taking advantages of the unique two-dimensional structures and outstanding properties of AL materials.<sup>1–3</sup> The interfaces between FM materials and conducting graphene play a dominant role in the spin injection in graphene-based devices, where the excellent spin transport properties of graphene are utilized.<sup>4–7</sup> Insulating hexagonal boron nitride (h-BN) can be utilized as a tunneling barrier of the magnetic tunneling junctions in magnetoresistive devices<sup>8–10</sup> and for the spin injection in graphene-based devices.<sup>9–11</sup> Since the performances of these nano-spintronic devices are quite sensitive to the interfacial properties,<sup>12</sup> the use of AL materials in these devices is quite reasonable. This is because AL materials allow us to fabricate interfaces with controlled microstructures and electronic and spintronic properties at the atomic level owing to the two-dimensional structural homogeneity of AL materials.

Recent studies on the heterostructures of FM metals and AL materials have highlighted a significant impact of the FM metal/AL material interfaces on the magnetic properties of FM metals as well as those of AL materials.<sup>13–17</sup> It has been shown that a local transition of the magnetization easy-axis from the in-plane to out-of-plane direction occurs in the

region near the graphene/Ni interface.<sup>15</sup> Recently, it has been reported that perpendicular magnetic anisotropy (PMA) is drastically enhanced in a Co thin film intercalated between graphene and Ir(111).<sup>16</sup> On the other hand, in the case of the FM metal/h-BN heterostructures, much less effort has been directed toward understanding the impact of the interfaces on the magnetic properties of FM metals. A recent theoretical study has predicted that the Co/h-BN interface can promote PMA of Co, even though the magnetic anisotropy energy (MAE) due to the Co/h-BN interface is smaller than that due to the Co/graphene interface and the free Co surface.<sup>17</sup>

In this study, we report a discovery of the interface-induced PMA in the Co nanoparticles (NPs) on h-BN prepared on Pt(111). The measurements of X-ray magnetic circular dichroism (XMCD) demonstrated that the FM Co NPs exhibit PMA at room temperature. From the depth-resolved analysis of XMCD at the Co  $L_{2,3}$ -edges, it was revealed that at the Co NP/h-BN interface the magnitude of the orbital magnetic moment ( $m_{\text{orb}}$ ) with respect to the spin magnetic moment ( $m_{\text{spin}}$ ) in the out-of-plane direction becomes larger than that in bulk Co. The near-edge X-ray absorption fine structure (NEXAFS) measurements at the B and N  $K$ -edges showed the orbital hybridization between Co and BN, which could bring about the  $m_{\text{orb}}$  enhancement contributing to the observed PMA.

Single-layer h-BN was prepared on a Pt(111) single crystal by chemical vapor deposition in an ultra-high vacuum

<sup>a)</sup>Authors to whom correspondence should be addressed: yamada@bk.tsukuba.ac.jp and sakai.seiji@qst.go.jp

(UHV) chamber (base pressure  $\sim 10^{-8}$  Pa). A clean Pt(111) surface was prepared by cycling  $\text{Ar}^+$  sputtering, annealing at  $600^\circ\text{C}$  in the  $\text{O}_2$  atmosphere, and short annealing at  $800^\circ\text{C}$  in UHV. By exposing the Pt(111) surface to 100 Langmuir of borazine ( $\text{B}_3\text{N}_3\text{H}_6$ ), while the substrate temperature was kept at  $800^\circ\text{C}$ , single-layer h-BN with complete surface coverage was synthesized as reported in a previous study.<sup>18</sup> Co was subsequently deposited on the h-BN surface at the substrate temperature of  $250^\circ\text{C}$  by using an electron beam evaporator. The deposition rate and nominal thickness of Co were controlled to  $\sim 0.02$  nm/min and  $\sim 1.5$  nm, respectively, by using a quartz crystal microbalance. The surface morphology of the sample was investigated by scanning tunneling microscopy (STM) and atomic force microscopy (AFM). The NEXAFS and XMCD experiments at the B  $K$ -edge, N  $K$ -edge, and Co  $L_{2,3}$ -edges were conducted *in situ* by using a depth-resolved XMCD chamber (base pressure  $\sim 10^{-8}$  Pa) installed on the soft X-ray beamline BL-7A of the Photon Factory, KEK.<sup>15,19</sup> The NEXAFS and XMCD measurements at the B  $K$ -edge, N  $K$ -edge, and Co  $L_{2,3}$ -edges were done at room temperature with circularly polarized X-ray beams (circular polarization factor  $P_c = 0.8$ ) in the partial electron yield (PEY) mode with retarding voltages of  $-100$  V,  $-300$  V, and  $-500$  V, respectively. The XMCD measurements were performed in remanence after applying a pulsed magnetic field ( $H = 700$  Oe and a pulse duration of  $\sim 5$  s) by Helmholtz coils. The concept of the depth-resolved X-ray absorption technique is schematically shown in Fig. 1(a). In the depth-resolved measurements, the mean probing depth ( $\lambda$ ) from the surface can be estimated from the mean escaping depth of the emitted Auger electrons, which changes depending on the emission angle  $\theta$  between the sample surface and the detection area on the imaging-type detector. In the analysis of the Co  $L_{2,3}$ -edge data,  $\lambda$  is estimated from the  $\lambda$ - $\theta$  relationship in an iron film<sup>19</sup> for the range of  $\theta \leq 15^\circ$  and under the reasonable assumption that  $\lambda$  is proportional to  $\sin \theta$  for the range of  $\theta > 15^\circ$ . The geometries used in the depth-resolved measurements are indicated in Fig. 1(b). Throughout this study, the incidence angles of the circularly polarized X-ray beams ( $\alpha$ ) and the pulsed magnetic fields ( $\beta$ ) to the sample surface were fixed to  $\alpha = 90^\circ$  and  $\beta = 90^\circ$  [the normal incidence (NI) condition, hereafter] and  $\alpha = 30^\circ$  and  $\beta = 0^\circ$  [the grazing incidence (GI) condition, hereafter]. In the XMCD sum rule analysis,<sup>20</sup> the magnetic dipole operator was neglected, and the 3d electron occupation number of Co was assumed to be the same as that of bulk Co (7.51).<sup>20</sup>

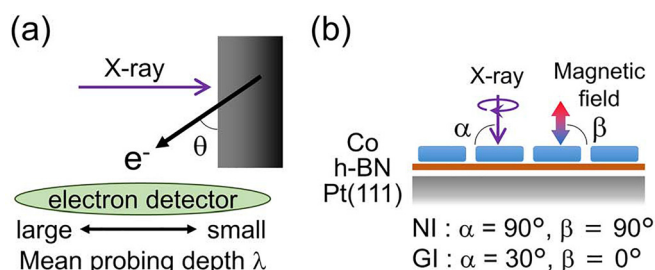


FIG. 1. (a) Concept of the depth-resolved X-ray absorption technique. (b) Experimental configuration of the depth-resolved NEXAFS and XMCD measurements.

Figure 2(a) shows the STM image of the single-layer h-BN on Pt(111). A moiré pattern of h-BN with a periodicity of  $\sim 2.5$  nm, which corresponds to the  $9 \times 9$  superstructure due to the lattice mismatch between epitaxial h-BN and the Pt(111) surface, is observed.<sup>18</sup> Extensive STM observations confirmed that the most of the Pt(111) surface is covered with the epitaxially grown h-BN. Figure 2(b) shows the AFM image of h-BN/Pt(111) after the Co deposition. Co atoms aggregate to NP as seen in the figure and its inset. Figure 2(c) presents a frequency distribution of the lateral diameter and height of Co NPs analyzed from the AFM image. The Co NPs have a broad size distribution with the mean diameter and height of  $\sim 20$  nm and  $\sim 1.6$  nm, respectively. Correlations are not observed between the diameters of the Co NPs and the periodicity of the moiré pattern of h-BN. As shown in the inset of Fig. 2(b), the Co NPs tend to show a hexagonal shape arranged in the same direction. This indicates that the Co NPs are single crystals with an epitaxial relationship with h-BN. It is considered that the almost perfect lattice matching between Co(0001) and h-BN makes the epitaxial growth of Co NPs more feasible.

Figures 3(a) and 3(b) show the B and N  $K$ -edge NEXAFS spectra of h-BN/Pt(111), respectively. The upper and lower curves in these figures show the data obtained under the NI and GI conditions, respectively. The prominent peaks labeled with  $\pi^*$  in each spectrum are attributed to the  $\pi^*$  resonances (B  $1s$ - $\pi^*$  and N  $1s$ - $\pi^*$  transitions) characteristic of h-BN. The spectral shapes are very similar to those of bulk h-BN, indicating the similar electronic structure of h-BN on Pt(111) to suspended h-BN due to the weak van der Waals type interaction at the h-BN/Pt(111) interface.<sup>21</sup> The strong angular dependence of the  $\pi^*$  peaks between the NI and GI conditions shows the flat growth of h-BN on the Pt(111) surface. In Fig. 3(b), a small shoulder A ( $\sim 398$  eV) is observed at the lower energy side of the  $\pi^*$  peak. This low energy shoulder A is ascribed to the adsorption-induced gap states of h-BN caused by the hybridization between the d orbitals of Pt and the  $\pi^*$  orbital of N of h-BN.<sup>21</sup> It was

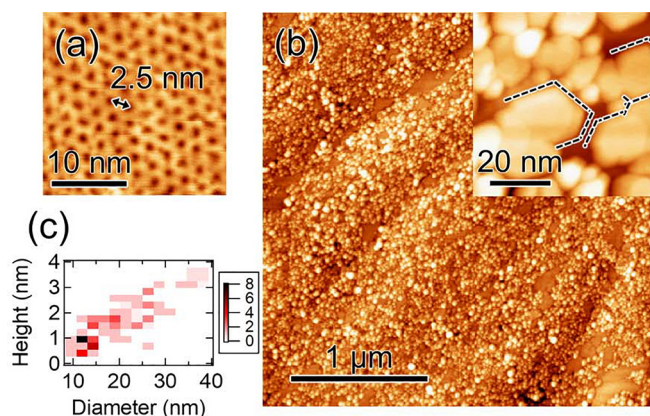


FIG. 2. (a) STM image of h-BN/Pt(111). Sample bias and tunneling current are 5.80 V and 83.5 pA, respectively. The bidirectional arrow on the image shows the periodicity of the moiré pattern of h-BN (2.5 nm). (b) Wide scan AFM image and narrow scan STM image (inset) of Co NPs/h-BN/Pt(111). The black dotted lines in the inset are drawn to guide the eyes. For the STM image, sample bias = 1.21 V and tunneling current = 88.9 pA. (c) Frequency distribution of the height and diameter of Co NPs in (b). The frequency is represented by the color of each point as indicated in the color bar.

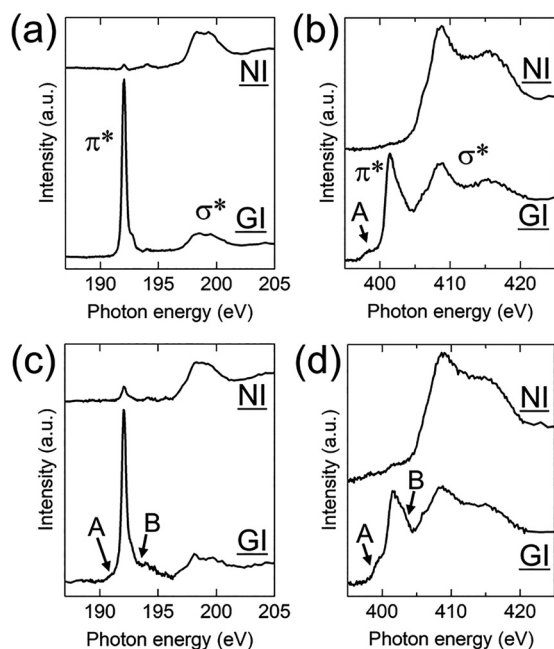


FIG. 3. (a) B and (b) N  $K$ -edge NEXAFS spectra of h-BN/Pt(111). (c) B and (d) N  $K$ -edge NEXAFS spectra of Co NPs/h-BN/Pt(111). The spectra obtained under the NI and GI conditions are shown in the upper and lower parts of each figure.  $\pi^*$  and  $\sigma^*$  show the peaks ascribed to the  $1s$ - $\pi^*$  and  $1s$ - $\sigma^*$  transitions in h-BN, respectively. The shoulders A and B can be attributed to the adsorption-induced gap states and the interlayer conduction band states, respectively (see text for details).

reported that this low energy shoulder develops into a peak in the spectrum of h-BN/Ni(111) in which a strong chemical bonding between N and Ni exists.<sup>21,22</sup> Figures 3(c) and 3(d) show the B and N  $K$ -edge NEXAFS spectra measured after the Co deposition, respectively. It is found that the intensity of the low energy shoulder A in the N  $K$ -edge NEXAFS spectrum [Fig. 3(d)] becomes more prominent and a low energy shoulder A ( $\sim 191$  eV) corresponding to the same adsorption-induced gap states appears in the B  $K$ -edge spectrum [Fig. 3(c)]. One can also see shoulders B at the higher energy side of the  $\pi^*$  peak in Figs. 3(c) and 3(d). These high energy shoulders B can be attributed to the interlayer conduction band states as reported for h-BN/Ni(111).<sup>21,22</sup> The above spectral features indicate a significant modification of the electronic structure of h-BN due to the hybridization between the h-BN  $\pi$  orbitals and the Co  $d$  orbitals at the Co NP/h-BN interface. The co-presence of the features attributed to the  $\pi$ - $d$  hybridized and pristine h-BN in the B and N  $K$ -edge spectra can be understood by the fact that the Co NPs do not cover the whole surface area of h-BN as seen in Fig. 2(b) and its inset.

Figure 4 shows the non-depth-resolved (PEY for simplicity) Co  $L_{2,3}$ -edge NEXAFS (red and blue curves) and XMCD (green curves) spectra of Co NPs/h-BN/Pt(111) obtained under the NI [Fig. 4(a)] and GI [Fig. 4(b)] conditions. The red and blue curves in the figures are the NEXAFS data measured in remanence after applying the pulsed magnetic fields parallel (red curves) and antiparallel (blue curves) to the photon helicity, respectively. The shapes of the NEXAFS spectra are almost identical to that of bulk Co.<sup>20</sup> A strong XMCD signal was detected only under the NI condition. This clearly shows that the FM Co NP on h-BN/

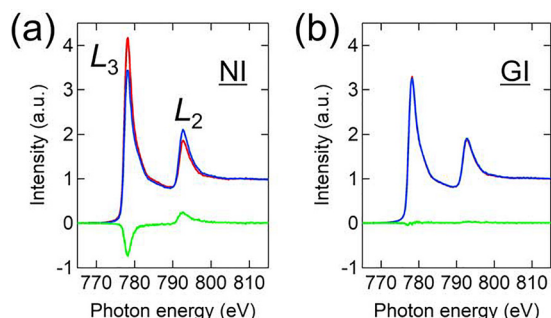


FIG. 4. Co  $L_{2,3}$ -edge NEXAFS and XMCD spectra of Co NPs/h-BN/Pt(111) under the (a) NI and (b) GI conditions. The red and blue curves in the figures show the NEXAFS spectra measured in remanence after applying the pulsed magnetic fields parallel and antiparallel to the photon helicity, respectively. The green curves show the XMCD spectra obtained from the difference in the NEXAFS spectra for the opposite magnetic field directions.

Pt(111) exhibits PMA at room temperature. The total magnetic moment ( $m_{\text{tot}}$ ) of Co evaluated from the PEY XMCD spectrum in Fig. 4(a) by applying the sum rules<sup>20</sup> is  $m_{\text{tot}} = 0.93 \mu_{\text{B}}/\text{atom}$  ( $m_{\text{spin}} = 0.80 \mu_{\text{B}}/\text{atom}$  and  $m_{\text{orb}} = 0.13 \mu_{\text{B}}/\text{atom}$ ) that is smaller than the one of bulk Co ( $1.7 \mu_{\text{B}}/\text{atom}$ ).<sup>20</sup>

In order to gain microscopic insights into the nature of the PMA in the FM Co NPs, we conducted a depth-resolved analysis of the Co  $L_{2,3}$ -edge XMCD spectra under the NI condition. As shown in Fig. 5(a), obvious changes are observed in the XMCD intensities with the mean probing depth  $\lambda$ . The effective spin magnetic moments  $m_{\text{spin}}$ , orbital magnetic moments  $m_{\text{orb}}$ , total magnetic moments  $m_{\text{tot}}$  in the out-of-plane direction, and the ratio of  $m_{\text{orb}}/m_{\text{spin}}$  obtained by using the sum rules are plotted in Figs. 5(b) and 5(c) as a function of  $\lambda$ . In Fig. 5(b), both  $m_{\text{spin}}$  and  $m_{\text{orb}}$  increase with the increase of  $\lambda$  toward the depth close to the Co NP/h-BN interface ( $\sim$ mean height of the Co NPs). This behavior is accounted for by taking the size distribution of the Co NPs [Fig. 2(c)] into consideration. The volume of the Co NP corresponding to the superparamagnetic (SPM) limit<sup>23,24</sup> is roughly estimated to be  $\sim 300 \text{ nm}^3$  from the magnetocrystalline anisotropy constant of hcp Co ( $4.5 \times 10^5 \text{ J/m}^3$ ).<sup>25</sup> Since the mean volume of the Co NPs ( $\sim 700 \text{ nm}^3$ ) in the present sample is close to the estimated value, it is considered that a small fraction of Co NPs within the size distribution as shown in Fig. 2(c) is SPM at room temperature. Note that the above simple estimation is to estimate the order of magnitude, and the surface/interface magnetic anisotropy and shape anisotropy of the Co NPs are neglected. In the depth-resolved Co  $L_{2,3}$ -edge measurements, the ratio of the NEXAFS signals from the SPM Co NPs becomes larger in the range that  $\lambda$  is less than or comparable to the height of the small SPM Co NPs ( $\sim 1 \text{ nm}$ ) as depicted in Fig. 5(d). Due to the contribution of these small SPM Co NPs which exhibit no remanent magnetization and XMCD signal, the estimated values of the magnetic moments at the small mean probing depth  $\lambda \lesssim 1 \text{ nm}$  can be remarkably small compared to those at the larger  $\lambda$  [Fig. 5(b)]. This also affects the relatively small moments even at the larger  $\lambda$  and in PEY XMCD compared to those in bulk Co. It is worthy to note that another Co NPs/h-BN/Pt(111) sample with a smaller mean diameter ( $\sim 10 \text{ nm}$ ) and thickness ( $\sim 1 \text{ nm}$ ) of Co NPs showed no

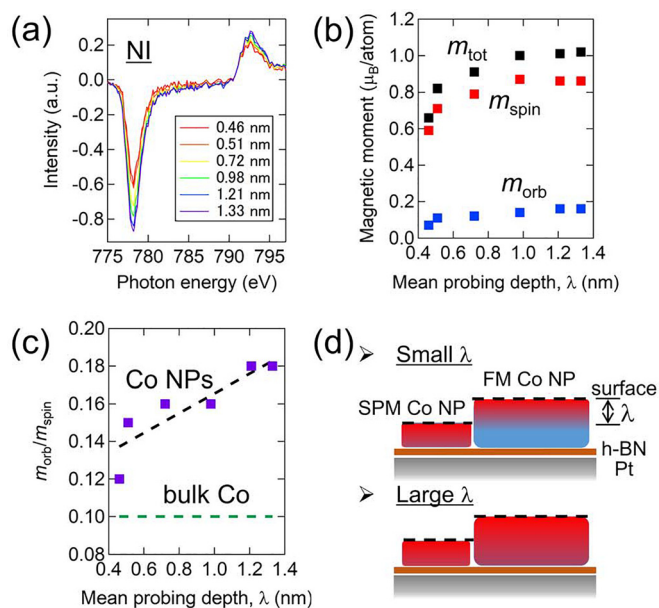


FIG. 5. (a) Depth-resolved Co  $L_{2,3}$ -edge XMCD spectra of Co NPs/h-BN/Pt(111) under the NI condition. The spectra at different mean probing depths  $\lambda$  are represented by different colors as indicated in the figure. (b) and (c) Mean probing depth dependences of (b) the magnetic moments;  $m_{\text{tot}}$ ,  $m_{\text{spin}}$ , and  $m_{\text{orb}}$  and (c) the  $m_{\text{orb}}/m_{\text{spin}}$  ratio for the FM Co NPs. The black dotted line is drawn to guide the eyes. (d) Schematic illustration representing the contributions of the small SPM Co NP and large FM Co NP to the depth-resolved NEXAFS signal. The red areas show the regions of the Co NP within the mean probing depth  $\lambda$ . The contribution of the SPM Co NPs in comparison to that of the FM Co NPs is large/small under the small/large  $\lambda$  conditions, respectively.

detectable XMCD in remanence (not shown), supporting the above discussion.

The analysis of the  $m_{\text{orb}}/m_{\text{spin}}$  ratio as a function of  $\lambda$  [Fig. 5(c)] allows us to investigate the nature of PMA in the FM Co NPs separately from the influence of the SPM Co NPs. In Fig. 5(c), the  $m_{\text{orb}}/m_{\text{spin}}$  ratio at the smallest mean probing depth ( $\lambda \sim 0.4$  nm) is close to that of bulk Co ( $m_{\text{orb}}/m_{\text{spin}} = 0.1$ ).<sup>20</sup> However, the  $m_{\text{orb}}/m_{\text{spin}}$  ratio becomes larger in the larger  $\lambda$  region ( $m_{\text{orb}}/m_{\text{spin}} \sim 0.18$ ). The large  $m_{\text{orb}}/m_{\text{spin}}$  ratio at the large  $\lambda$  indicates that the orbital magnetic moment  $m_{\text{orb}}$  in the out-of-plane direction is largely enhanced in the vicinity of the Co NP/h-BN interface. A simple estimation considering the contribution from a certain depth in the FM Co NP to the depth-resolved NEXAFS data<sup>26</sup> and the thickness distribution of the Co NPs gives the  $m_{\text{orb}}/m_{\text{spin}}$  ratio of  $\sim 0.3$  just above the Co/h-BN interface. As the magnetic anisotropy due to the spin-orbit interaction is directly linked to anisotropy of the orbital magnetic moment,<sup>27</sup> this interface-induced  $m_{\text{orb}}$  enhancement can be closely related to the PMA in the FM Co NPs. Recent theoretical calculations have suggested that in the Co/h-BN heterostructure, the Co/h-BN interface can promote PMA of Co depending on the degree of hybridization between the h-BN  $\pi$  orbitals and the Co  $d$  orbitals in a similar manner to the Co/graphene heterostructure, although the interface-induced MAE in the Co/h-BN heterostructure is smaller than that in the Co/graphene heterostructure and the MAE induced by the free Co surface.<sup>17</sup> The very small lattice mismatch between Co(0001) and h-BN at the interface (0.4%) and also the epitaxial growth of Co NPs on h-BN can lead to the strong hybridization as proved by the B and N  $K$ -edge NEXAFS measurements.

Although the precise mechanism of the  $m_{\text{orb}}$  enhancement at the Co NP/h-BN interface is not yet very obvious, the present finding shows clearly that h-BN indeed induces visible PMA in FM metal/h-BN heterostructures. Further studies on the Co thickness dependence and on Co NPs/graphene/Pt(111) for comparison are required to gain quantitative information on the effect of the Co/h-BN interface on the PMA behavior.

In summary, the present study demonstrated that the FM Co NPs grown on h-BN/Pt(111) show PMA at room temperature. The depth-resolved analysis of the Co  $L_{2,3}$ -edge XMCD spectra revealed a significant increase of the  $m_{\text{orb}}/m_{\text{spin}}$  ratio along the out-of-plane direction as the mean probing depth from the sample surface approaches the mean height of the Co NPs. It was shown from the B and N  $K$ -edge NEXAFS spectra that there exists orbital hybridization between the BN  $\pi$  orbital and the Co  $d$  orbital at the Co NPs/h-BN interface, as a possible origin of the PMA. The present finding would shed light on the applications of FM metal/h-BN heterostructures to the spintronic devices such as magnetic random access memory and magnetoresistive sensors utilizing h-BN as a tunneling barrier and insulating substrate.

The authors acknowledge Professor Pavel Avramov (Kyungpook National University) and Dr. Atsuo Kawasuso (QST) for useful discussions and theoretical supports. This work was partly supported by JSPS KAKENHI (Grant Nos. JP26286011, JP16H03875, JP16K13678, JP17H07376, and JP17H07376). The part of the work was performed under the approval of the Photon Factory Program Advisory Committee (Proposal Nos. 2016G539 and 2017G030). Z.I.P. and P.B.S. acknowledge the financial supports of the Ministry of Education and Science of the Russian Federation in the framework of Increase Competitiveness Program of NUST «MISiS» (No. K2-2017-001). P.B.S. acknowledges the financial support of the RFBR, according to the research project (No. 16-32-60138 mol\_a\_dk).

<sup>1</sup>W. Han, R. K. Kawakami, M. Gmitra, and J. Fabian, *Nat. Nanotechnol.* **9**, 794 (2014).

<sup>2</sup>Y. P. Feng, L. Shen, M. Yang, A. Wang, M. Zeng, Q. Wu, S. Chintalapati, and C.-R. Chang, *WIREs Comput. Mol. Sci.* **7**, e1313 (2017).

<sup>3</sup>D. Sander, S. O. Valenzuela, D. Makarov, C. H. Marrows, E. E. Fullerton, P. Fischer, J. McCord, P. Vavassori, S. Mangin, P. Pirro, B. Hillebrands, A. D. Kent, T. Jungwirth, O. Gutflisch, C. G. Kim, and A. Berger, *J. Phys. D: Appl. Phys.* **50**, 363001 (2017).

<sup>4</sup>C. Vo-Van, Z. Kassir-Bodon, H. Yang, J. Coraux, J. Vogel, S. Pizzini, P. Bayle-Guillemaud, M. Chshiev, L. Ranno, V. Guisset, P. David, V. Salvador, and O. Fruchart, *New J. Phys.* **12**, 103040 (2010).

<sup>5</sup>M. V. Kamalakar, C. Groenvelde, A. Dankert, and S. P. Dash, *Nat. Commun.* **6**, 6766 (2015).

<sup>6</sup>S. Entani, H. Naramoto, and S. Sakai, *J. Appl. Phys.* **117**, 17A334 (2015).

<sup>7</sup>S. Sakai, S. Majumdar, Z. I. Popov, P. V. Avramov, S. Entani, Y. Hasegawa, Y. Yamada, H. Huhtinen, H. Naramoto, P. B. Sorokin, and Y. Yamauchi, *ACS Nano* **10**, 7532 (2016).

<sup>8</sup>S. V. Faleev, S. S. P. Parkin, and O. N. Mryasov, *Phys. Rev. B* **92**, 235118 (2015).

<sup>9</sup>V. M. Karpan, P. A. Khomyakov, G. Giovannetti, A. A. Starikov, and P. J. Kelly, *Phys. Rev. B* **84**, 153406 (2011).

<sup>10</sup>A. M. Ukpong, *J. Phys.: Condens. Matter* **29**, 285302 (2017).

<sup>11</sup>T. Yamaguchi, Y. Inoue, S. Masubuchi, S. Morikawa, M. Onuki, K. Watanabe, T. Taniguchi, R. Moriya, and T. Machida, *Appl. Phys. Express* **6**, 073001 (2013).

<sup>12</sup>B. Dlubak, P. Seneor, A. Anane, C. Barraud, C. Deranlot, D. Deneuve, B. Servet, R. Mattana, F. Petroff, and A. Fert, *Appl. Phys. Lett.* **97**, 092502 (2010).

- <sup>13</sup>S. Entani, M. Kurahashi, X. Sun, and Y. Yamauchi, *Carbon* **61**, 134 (2013).
- <sup>14</sup>M. Ohtomo, Y. Yamauchi, A. A. Kuzubov, N. S. Eliseeva, P. V. Avramov, S. Entani, Y. Matsumoto, H. Naramoto, and S. Sakai, *Appl. Phys. Lett.* **104**, 051604 (2014).
- <sup>15</sup>Y. Matsumoto, S. Entani, A. Koide, M. Ohtomo, P. V. Avramov, H. Naramoto, K. Amemiya, T. Fujikawa, and S. Sakai, *J. Mater. Chem. C* **1**, 5533 (2013).
- <sup>16</sup>H. Yang, A. D. Vu, A. Hallal, N. Rougemaille, J. Coraux, G. Chen, A. K. Schmid, and M. Chshiev, *Nano Lett.* **16**, 145 (2016).
- <sup>17</sup>B. S. Yang, J. Zhang, L. N. Jiang, W. Z. Chen, P. Tang, X.-G. Zhang, Y. Yan, and X. F. Han, *Phys. Rev. B* **95**, 174424 (2017).
- <sup>18</sup>E. Čavar, R. Westerström, A. Mikkelsen, E. Lundgren, A. S. Vinogradov, M. L. Ng, A. B. Preobrajenski, A. A. Zakharov, and N. Mårtensson, *Surf. Sci.* **602**, 1722 (2008).
- <sup>19</sup>K. Amemiya, S. Kitagawa, D. Matsumura, T. Yokoyama, and T. Ohta, *J. Phys.: Condens. Matter* **15**, S561 (2003).
- <sup>20</sup>C. T. Chen, Y. U. Idzerda, H.-J. Lin, N. V. Smith, G. Meigs, E. Chaban, G. H. Ho, E. Pellegrin, and F. Sette, *Phys. Rev. Lett.* **75**, 152 (1995).
- <sup>21</sup>A. B. Preobrajenski, S. A. Krasnikov, A. S. Vinogradov, M. L. Ng, T. Käämbre, A. A. Cafolla, and N. Mårtensson, *Phys. Rev. B* **77**, 085421 (2008).
- <sup>22</sup>A. B. Preobrajenski, A. S. Vinogradov, and N. Mårtensson, *Phys. Rev. B* **70**, 165404 (2004).
- <sup>23</sup>S. H. Charap, P.-L. Lu, and Y. He, *IEEE Trans. Magn.* **33**, 978 (1997).
- <sup>24</sup>M. Yu, M. F. Doerner, and D. J. Sellmyer, *IEEE Trans. Magn.* **34**, 1534 (1998).
- <sup>25</sup>P. Gambardella, S. Rusponi, M. Veronese, S. S. Dhesi, C. Grazioli, A. Dallmeyer, I. Cabria, R. Zeller, P. H. Dederichs, K. Kern, C. Carnone, and H. Brune, *Science* **300**, 1130 (2003).
- <sup>26</sup>K. Amemiya, *Phys. Chem. Chem. Phys.* **14**, 10477 (2012).
- <sup>27</sup>P. Bruno, *Phys. Rev. B* **39**, 865 (1989).